Applied Mathematical Modelling 33 (2009) 4283–4302

Contents lists available at ScienceDirect

Applied Mathematical Modelling

journal homepage: www.elsevier.com/locate/apm

The trajectory and stability of a spiralling liquid jet: Viscous theory

S.P. Decent [a,*], A.C. King [a], M.J.H. Simmons [b], E.I. Părău [c], I.M. Wallwork [a], C.J. Gurney [a], J. Uddin [a]

[a] School of Mathematics, The University of Birmingham, Edgbaston, Birmingham B15 2TT, UK
[b] Department of Chemical Engineering, The University of Birmingham, Edgbaston, Birmingham B15 2TT, UK
[c] School of Mathematics, University of East Anglia, Norwich NR4 7TJ, UK

ARTICLE INFO

Article history:
Received 21 November 2007
Received in revised form 27 February 2009
Accepted 9 March 2009
Available online 18 March 2009

Keywords:
Rotation
Jet
Stability
Surface tension
Viscous

ABSTRACT

We examine a spiralling slender viscous jet emerging from a rapidly rotating orifice, extending Wallwork et al. [I.M. Wallwork, S.P. Decent, A.C. King, R.M.S.M. Schulkes, The trajectory and stability of a spiralling liquid jet. Part 1. Inviscid theory, J. Fluid Mech. 459 (2002) 43–65] by incorporating viscosity. The effects of viscosity on the trajectory of the jet and its linear instability are determined using a mixture of computational and asymptotic methods, and verified using experiments. A non-monotonic relationship between break-up length and rotation rate is demonstrated with the trend varying with viscosity. The sizes of the droplets produced by this instability are determined by considering the most unstable wave mode. It is also found that there is a non-monotonic relationship between droplet size and viscosity. Satellite droplet formation is also considered by analysing very short wavelength modes. The effects of long wavelength modes are examined, and a wave which propagates down the trajectory of the jet is identified for the highly viscous case. A comparison between theoretical and experimental results is made, with favourable agreement. In particular, a quantitative comparison is made between droplet sizes predicted from the theory with experimental observations, with encouraging agreement obtained. Four different types of break-up are identified in our experiments. The experimentally observed break-up mechanisms are discussed in light of our theory.

1. Introduction

In Wallwork et al. [1] we presented asymptotic and numerical results for an inviscid liquid emerging from a rapidly rotating container. Experimental results were given for a low viscosity liquid, showing good agreement between theory and experimental data. This work has applications to prilling [2] which is a common industrial technique for producing pellets (for example, fertiliser and magnesium pellets). In this process thousands of liquid jets emerge from a specially perforated rapidly rotating drum. Each jet follows a curved trajectory and breaks up into droplets due to a surface tension driven instability. These droplets cool and solidify forming pellets. There are numerous economic reasons for wanting to control this instability process (including the optimization of the process, the uniformity of the product, and the minimization of satellite drop formation to decrease waste). We wish to control this instability by forcing the jet at the orifice by using a vibration (either by vibrating the nozzle or using acoustic insonification), and this will force the jet giving droplets of a desired size. However, this cannot be done until a thorough understanding of the instability has been achieved.

Previous work presented on this prilling scenario has examined inviscid liquids [1,3,4]. However, in industrial settings, the liquids used are viscous. Typically, liquids used in prilling have viscosities ranging over approximately $10^{-3} - 10^{0}$ kg m^{-1} s^{-1}, and the rotation rate of the drum is typically several hundred revolutions per minute or more.

* Corresponding author. Tel.: +44 121 414 7566.
E-mail address: d.p.decent@bham.ac.uk (S.P. Decent).

0307-904X/$ - see front matter © 2009 Elsevier Inc. All rights reserved.
doi:10.1016/j.apm.2009.03.011

There is previous work detailing viscous jets, namely experimental work presented by Partridge et al. [5] and non-linear analysis presented by Părău et al. [6]. In Părău et al. [6] many assumptions were made. It was assumed that the trajectory of the jet can be computed without considering the viscosity of the liquid, and it was assumed that waves on the jet were always long when compared to the radius of the jet. In addition, it was assumed that the unstable waves always propagate away from the orifice and never towards the orifice. It was also assumed that the instability can always be described using a temporal rather than a spatial instability approach. These four assumptions are not made here, and instead we take a more careful look at the influence of viscosity on the jet. We shall find circumstances in which the assumptions made in Părău et al. [6] were realistic, but others in which they are not. We concentrate on the Newtonian model for viscosity here due to the complexity of the equations produced even in this situation, though non-Newtonian models are of considerable engineering interest and will be considered in future publications.

Rayleigh [7] and Weber [8] incorporated viscosity into the linear instability calculation for a straight jet. Here we firstly determine the effect of viscosity on the trajectory of our curved jets, and then apply the methods of Rayleigh and Weber to determine the viscous instability of our curved jets. We will also follow the spatial stability methodology of Keller et al. [9], before presenting some experimental results for viscous Newtonian liquids. We consider short and long wavelength modes, main and satellite drop formation, and the break-up length in detail. We also discuss the dynamics of break-up and identify four different types of break-up.

Other works on curved liquid sheets and jets are summarised and referenced in part I of this work [1]. Important works include Tuck [10], Vanden-Broeck and Keller [11], Entov and Yarin [12], Dias and Vanden-Broeck [13], Yarin [14] and Cummings and Howell [15]. In particular, Dias and Vanden-Broeck [13] investigated steady two-dimensional inviscid solutions with gravity, determining the trajectory of the flow, and Cummings and Howell [15] investigated nearly straight slender viscous fluid fibres arising in extrusion problems.

2. The equations of motion

We consider a circular cylindrical container of radius s_0 rotating about its axis with rotation rate Ω. A viscous jet emerges from an orifice on the curved surface of the cylinder. This is the scenario in industrial prilling.

We derive non-dimensional equations of motion following Wallwork et al. [1] but incorporating viscosity. We work in a rotating reference frame in which the orifice is fixed. If g is the acceleration due to gravity and s_0 is the radius of the drum, then we assume that $s_0\Omega^2 \gg g$ so that the jets do not fall significantly out of plane before breaking up into drops. This is a reasonable assumption to make as we are modelling jets emerging from a rapidly rotating cylinder used in the prilling process, and so the effect of rotation is much larger than that of gravity. We use a curvilinear coordinate system (s, n, ϕ) where s is the arclength along the centreline of the jet from the orifice, and (n, ϕ) are plane polar coordinates in any cross-section of the jet. The centreline of the jet is at $X\mathbf{i} + Z\mathbf{k}$ where $\mathbf{i}$ and $\mathbf{k}$ are unit vectors in Cartesian coordinates, with the origin $X = Z = 0$ at the centre of the orifice, where the x-axis is directed normal to the surface of the container in the initial direction of the jet and the z-axis is orthogonal to the x-axis in the plane of the centreline of the jet. The positive z-axis points in the opposite direction to the motion of the container. Also, $X = X(s,t)$ and $Z = Z(s,t)$ where t is time. The y-axis is in the same direction as the axis of the cylinder, so the centreline of the jet lies in the plane $y = 0$.

We non-dimensionalise using the transformations

$$\begin{aligned} &\bar{u} = \frac{u}{U}, \quad \bar{v} = \frac{v}{U}, \quad \bar{w} = \frac{w}{U}, \quad \bar{p} = \frac{p}{\rho U^2}, \quad \bar{n} = \frac{n}{a}, \quad \epsilon = \frac{a}{s_0}, \\ &\bar{R} = \frac{R}{a}, \quad \bar{s} = \frac{s}{s_0}, \quad \bar{t} = \frac{tU}{s_0}, \quad \bar{X} = \frac{X}{s_0}, \quad \bar{Z} = \frac{Z}{s_0}, \end{aligned} \tag{1}$$

where U is the exit speed of the jet in the rotating frame, ρ is the liquid density, a the radius of the orifice, ϵ is an aspect ratio, p is the pressure, R is the jet radius and u, v and w are the tangential, radial and azimuthal velocity components relative to the centreline of the jet, respectively. The bars denote dimensionless quantities in the above expressions. Then the jet velocity is $\mathbf{u} = u\mathbf{e}_s + v\mathbf{e}_n + w\mathbf{e}_\phi$, where $\mathbf{e}_s$ is the unit vector tangential to the jet's centreline, and $\mathbf{e}_n$ and $\mathbf{e}_\phi$ are the usual plane polar coordinate unit vectors in any cross-section of the jet.

We drop the overbars and derive the continuity equation, the Navier–Stokes equations, with the kinematic condition, tangential and normal stress conditions on the jet's surface $n = R(s, \phi, t)$ in this coordinate system. (The equations are written out in full in Părău et al. [6]).

We also have an arclength condition which is

$$X_s^2 + Z_s^2 = 1, \tag{2}$$

since s is the arclength along the centreline and subscripts in s refer to derivatives with respect to s. In addition we have

$$v = w = 0 \quad \text{on } n = 0, \tag{3}$$

since on the centreline of the jet at $n = 0$ there must be purely tangential flow.

The initial conditions at the orifice $(s = 0)$ are $X = Z = Z_s = 0, X_s = 1, R = 1$ and $u = 1$. The dimensionless parameters are the Weber number $We = \rho U^2 a/\sigma$, the Rossby number $Rb = U/(s_0\Omega)$, the aspect ratio $\epsilon = a/s_0$ (which we choose to be small

and base our asymptotics on it: this will correspond to a slender jet) and the Ohnesorge number $Oh = \mu/\sqrt{\sigma a \rho}$, where σ is the surface tension of the liquid and μ is the liquid's viscosity. The rotation rate of the drum is Ω. Note that we choose the lengthscale in our viscous parameter Oh to be a rather than s_0 so that this represents viscous shear across the width of the jet. Typical values for industrial scale prilling are $0 < Oh < 3$, $0.01 < Rb < 1, 10 < We < 1000$, and $\epsilon \approx 0.01$.

3. Asymptotic form of the steady state solutions

In Wallwork et al. [1] an inviscid steady jet trajectory and steady expressions were obtained for the velocity, pressure and jet radius based upon a regular slender jet asymptotic expansion using $0 < \epsilon \ll 1$. We here extend this calculation to include viscosity.

We take $w = 0$ so that is there is no velocity component in the azimuthal direction (no swirl), as in Wallwork et al. [1]. We apply the steady slender jet expansions from Wallwork et al. [1], namely

$$\left.\begin{aligned} &\mathbf{u} = \mathbf{u_0}(s) + \epsilon \mathbf{u_1}(s,n,\phi) + O(\epsilon^2),\\ &p = p_0(s,n,\phi) + \epsilon p_1(s,n,\phi) + O(\epsilon^2),\\ &R = R_0(s) + \epsilon R_1(s,\phi) + O(\epsilon^2),\\ &\mathbf{X} = \mathbf{X_0}(s) + \epsilon \mathbf{X_1}(s) + O(\epsilon^2), \end{aligned}\right\} \tag{4}$$

where $\mathbf{u}_i = u_i \mathbf{e}_s + v_i \mathbf{e}_n$, $v_0 = 0$, and $\mathbf{X_i} = X_i \mathbf{i} + Z_i \mathbf{k}$ for $i = 0, 1, \ldots$ For simplicity of notation, we write the leading-order components X_0 and Z_0 as X and Z, respectively. We obtain the leading-order equations

$$n\frac{du_0}{ds} + v_1 + n\frac{\partial v_1}{\partial n} = 0, \tag{5}$$

$$u_0\frac{du_0}{ds} = -\frac{\partial p_0}{\partial s} + \frac{1}{Rb^2}((X+1)X_s + ZZ_s) + \frac{Oh}{We^{1/2}}\left(\frac{1}{n}\frac{\partial u_1}{\partial n} + \frac{\partial^2 u_1}{\partial n^2} + \frac{1}{n^2}\frac{\partial^2 u_1}{\partial \phi^2}\right), \tag{6}$$

$$\frac{\partial p_0}{\partial n} = 0, \tag{7}$$

$$-\cos\phi(X_sZ_{ss} - X_{ss}Z_s)u_0^2 = -\frac{\partial p_1}{\partial n} - \frac{2u_0\cos\phi}{Rb} + \frac{\cos\phi}{Rb^2}((X+1)Z_s - ZX_s) + \frac{Oh}{We^{1/2}}\left(\frac{1}{n}\frac{\partial v_1}{\partial n} + \frac{\partial^2 v_1}{\partial n^2} + \frac{1}{n^2}\left(-v_1 + \frac{\partial^2 v_1}{\partial \phi^2}\right)\right), \tag{8}$$

$$\frac{\partial p_0}{\partial \phi} = 0, \tag{9}$$

$$\sin\phi(X_sZ_{ss} - X_{ss}Z_s)u_0^2 = -\frac{1}{n}\frac{\partial p_1}{\partial \phi} + \frac{2u_0\sin\phi}{Rb} + \frac{\sin\phi}{Rb^2}(ZX_s - (X+1)Z_s) + \frac{Oh}{We^{1/2}}\left(\frac{2}{n^2}\frac{\partial v_1}{\partial \phi}\right), \tag{10}$$

$$u_0\frac{dR_0}{ds} = v_1 \quad \text{on } n = R_0, \tag{11}$$

$$\frac{\partial u_1}{\partial n} = u_0\cos\phi(X_sZ_{ss} - X_{ss}Z_s) \quad \text{on } n = R_0, \tag{12}$$

$$p_0 = \frac{1}{nWe} \quad \text{on } n = R_0, \tag{13}$$

$$p_1 - \frac{2Oh}{We^{1/2}}\frac{\partial v_1}{\partial n} = \frac{1}{We}\left(-\frac{1}{R_0^2}\left(R_1 + \frac{\partial^2 R_1}{\partial \phi^2}\right) + \cos\phi(X_sZ_{ss} - X_{ss}Z_s)\right) \quad \text{on } n = R_0, \tag{14}$$

$$v_1 = 0 \quad \text{on } n = 0, \tag{15}$$

$$X_s^2 + Z_s^2 = 1. \tag{16}$$

We can define a Reynolds number $Re = \sqrt{We}/Oh = \rho U a/\mu$ and $Re = O(1)$. Therefore $\widetilde{Re} = Re/\epsilon = \rho U s_0/\mu = O(\epsilon^{-1})$. Hence we are in a high Reynolds number limit for Reynolds numbers based on arclengths of order s_0. This scaling for viscosity used in this paper is necessary so that in the following section we will obtain a linear dispersion relation for unsteady travelling waves that is a curved jet generalisation of the classical straight viscous jet result of Weber [8]. This results in viscous terms in (5)–(16) as shown above. However, we will show that these equations actually produce at leading-order the same trajectory as in the inviscid case given by Wallwork et al. [1].

From the continuity equations (5) and (15) we obtain $v_1 = -(n/2)(du_0/ds)$. Substituting this expression for v_1 into Eqs. (8) and (10), we find that the viscous terms on the right hand sides of these equations become identically equal to zero. Therefore viscosity now only appears in the above equations in (6) and (14). We can rewrite (6) as

$$f(s) = \nabla_{n,\phi}^2 u_1, \tag{17}$$

where

$$\nabla^2_{n,\phi} = \frac{1}{n}\frac{\partial}{\partial n} + \frac{\partial^2}{\partial n^2} + \frac{1}{n^2}\frac{\partial^2}{\partial \phi^2}$$

is the in-plane Laplacian operator. Eqs. (7) and (9) imply that $p_0 = p_0(s)$. In (17), $f(s) = We^{1/2}(u_0 du_0/ds + dp_0/ds - ((X+1)X_s + ZZ_s)/Rb^2)/Oh$.

We therefore have to solve (17) subject to boundary condition (12). This is a Neumann problem on a circular domain, where s is a parameter. To determine a solvability condition we multiply Eq. (17) by $\hat{u}(s,n,\phi)$ and integrate the result over the domain of interest S $(0 \leqslant n \leqslant R_0, 0 \leqslant \phi \leqslant 2\pi)$ giving

$$\int\int_S \hat{u}\nabla^2_{n,\phi} u_1 \, dS = \int\int_S \hat{u} f(s)\, dS, \tag{18}$$

where $\hat{u}$ satisfies the homogeneous Neumann problem, so that

$$\nabla^2_{n,\phi}\hat{u} = 0 \quad \text{with} \quad \frac{\partial \hat{u}}{\partial n} = 0 \quad \text{on } n = R_0. \tag{19}$$

Green's identity gives

$$\int\int_S \hat{u}\nabla^2_{n,\phi} u_1 \, dS = \int_B \hat{u}\frac{\partial u_1}{\partial n}\, dB, \tag{20}$$

where B is the boundary of S. From (12), (18) and (20) we obtain

$$\int_0^{2\pi}\int_0^{R_0} \hat{u} n f(s) dn\, d\phi = \int_0^{2\pi}\left[\hat{u}\frac{\partial u_1}{\partial n}\right]_{n=R_0} R_0\, d\phi = \int_0^{2\pi} [\hat{u}]_{n=R_0} R_0 g(s)\cos\phi\, d\phi, \tag{21}$$

where $g(s) = u_0(X_s Z_{ss} - X_{ss}Z_s)$. The general solution to (19) which is bounded in $0 \leqslant n \leqslant R_0$ and also periodic in ϕ with period 2π is simply $\hat{u} = \gamma(s)$, for some function $\gamma(s)$. Therefore (21) gives $\gamma(s) f(s) R_0^2 = 0$. But the jet radius R_0 cannot be zero. Since $\hat{u} = \gamma(s)$ is the general solution to the homogeneous problem, we must then have $f(s) = 0$ for all s. Therefore (6) and (12) give rise to two equations: namely $f(s) = 0$ and $\nabla^2_{n,\phi} u_1 = 0$. We note that neither of these expressions contain viscosity.

Finally, if we perform the calculation $\sin\phi(8) + \cos\phi(10)$ we obtain

$$\sin\phi\frac{\partial p_1}{\partial n} + \cos\phi\frac{1}{n}\frac{\partial p_1}{\partial \phi} = 0. \tag{22}$$

The boundary condition for this equation is (14). Once (22) is solved for p_1, (14) can then be viewed as a differential equation for R_1. But R_1 must be periodic in ϕ with period 2π. Consequently, the $\cos\phi(X_s Z_{ss} - X_{ss}Z_s)/We$ term in (14), which would otherwise cause $\phi\sin\phi$ type behaviour in R_1, must be balanced from a contribution in p_1 to avoid this non-periodic solution for R_1. Hence the solution to (22) and (14) is therefore

$$p_1 = \frac{n}{WeR_0}\cos\phi(X_s Z_{ss} - X_{ss}Z_s) + h_1(s) - \frac{Oh}{We^{1/2}}\frac{du_0}{ds} \tag{23}$$

and $R_1 = g_1(s)\cos\phi + g_2(s)\sin\phi + g_3(s)$ where $h_1(s), g_1(s), g_2(s)$ and $g_3(s)$ are arbitrary functions of s which could be found at next-order in this asymptotic expansion in ϵ. Note that p_1 only appears as derivatives with respect to n and ϕ in Eqs. (8) and (10), respectively. Therefore, from substituting (23) into (8) and (10), we see that we obtain no viscous contribution to the leading-order trajectory from p_1, since the term in (23) which is dependent on the Ohnesorge number is dependent on s only and not on n or ϕ. Therefore we have shown that the viscous terms vanish in (5)–(16), and we find the same leading-order problem for the trajectory here as in the inviscid case in Wallwork et al. [1]. (These leading-order equations are given in Appendix.) Hence viscosity does not affect the steady solution at leading-order, except in a viscous correction to p_1 in (23) which does not affect the leading-order trajectory, velocity, pressure or jet radius. This means that the slender jet approximation in this case results in no shear across the jet, except at higher-order.

So viscosity does not affect the leading-order *steady* solution. But we would like to know how the trajectory of this jet is affected by viscosity at higher-order. We therefore proceed to next-order to find the viscous correction to the steady trajectory by finding X_1 and Z_1.

We solve this problem following the same methodology outlined already in this section, but at next-order in ϵ. Similar solvability condition arguments apply at next-order. Naturally the algebraic manipulations are tedious and the equations all very lengthy, and we feel that to give details here would not add any insight. The details are available in Wallwork [16]. The equations after considerable work become

$$g_1^2 = \frac{WeR_0^4}{6}\left(\left(2u_0^2 + \frac{1}{R_0 We}\right)(X_s Z_{ss} - X_{ss}Z_s)^2 - \frac{4}{Rb}u_0(X_s Z_{ss} - X_{ss}Z_s) - \frac{1}{Rb^2}((ZX_s - (X+1)Z_s)(X_s Z_{ss} - X_{ss}Z_s) - 1)\right) \tag{24}$$

and

$$\left(u_0^2-\frac{1}{R_0}\right)(X_{1_s}Z_{ss}+X_sZ_{1_{ss}}-X_{1_{ss}}Z_s-X_{ss}Z_{1_s})=\frac{1}{R_0}\left(2g_1-\frac{1}{We}(X_sZ_{ss}-X_{ss}Z_s)\right)+\frac{1}{Rb^2}(Z_1X_s+ZX_{1_s}-X_1Z_s-(X+1)Z_{1_s})$$
$$+\frac{Oh}{We^{1/2}}\left(\frac{17}{6}\frac{du_0}{ds}(X_sZ_{ss}-X_{ss}Z_s)-\frac{1}{3}u_0(X_sZ_{sss}-X_{sss}Z_s)\right), \tag{25}$$

where $X_1(s)$ and $Z_1(s)$ are the $O(\epsilon)$ corrections to the leading-order components of the expansions in X and Z, and X and Z in (24) and (25) are short-hand for X_0 and Z_0, respectively. The above two equations must be solved simultaneously with the arclength condition (2) to $O(\epsilon)$ which is

$$X_sX_{1s}+Z_sZ_{1s}=0. \tag{26}$$

The initial conditions are $X_1=Z_1=X_{1_s}=Z_{1_s}=0$ at $s=0$. We solve the differential equations (24)–(26) numerically. These numerical solutions give the correction to the centreline caused by viscosity, and the trajectory is given by $(X+\epsilon X_1,0,Z+\epsilon Z_1)$.

Fig. 1 shows the trajectory of the centreline containing terms from both leading-order and next-order for various values of the Ohnesorge number. We can see from the graphs that increasing viscosity has the effect of making the jets more tightly coiled, though the leading-order solution acts as a very good approximation to the trajectory until large values of the arc-length s, unless Oh is large. However Oh is small or $O(1)$ for most liquid jets, since if $Oh\gg 1$ then it is difficult to form a jet in experiments [17].

4. Linear instability of the steady state solutions: Short waves

Using a multiple scales approach, we pose the expansions

$$\left.\begin{aligned}\mathbf{u}&=\bar{\mathbf{u}}(s,n,\phi,\epsilon)+\delta\tilde{\mathbf{u}}(s,\bar{s},n,\phi,t,\bar{t}),\\ R&=\bar{R}(s,\phi,\epsilon)+\delta\tilde{R}(s,\bar{s},\phi,t,\bar{t}),\\ p&=\bar{p}(s,n,\phi,\epsilon)+\delta\tilde{p}(s,\bar{s},n,\phi,t,\bar{t}),\\ \mathbf{X}&=\bar{\mathbf{X}}(s,\epsilon)+\delta\epsilon\tilde{\mathbf{X}}(s,\bar{s},t,\bar{t}),\end{aligned}\right\} \tag{27}$$

where $(\bar{\mathbf{u}},\tilde{\mathbf{u}})=(\bar{u},\tilde{u})\mathbf{e_s}+(\bar{v},\tilde{v})\mathbf{e_n}+(\bar{w},\tilde{w})\mathbf{e}_{\phi}$, $(\bar{\mathbf{X}},\tilde{\mathbf{X}})=(\bar{X},\tilde{X})\mathbf{i}+(\bar{Z},\tilde{Z})\mathbf{k}$ and δ is a small dimensionless parameter which measures the size of the unsteady disturbances as in Wallwork et al. [1]. (We note that we first tried $\mathbf{X}=\bar{\mathbf{X}}(s,\epsilon)+\delta\tilde{\mathbf{X}}_{\mathbf{0}}(s,\bar{s},t,\bar{t})+\delta\epsilon\tilde{\mathbf{X}}(s,\bar{s},t,\bar{t})$, but $\tilde{\mathbf{X}}_{\mathbf{0}}$ was found to be identically equal to zero). Here $\bar{s}=s/\epsilon$ is a short lengthscale and $\bar{t}=t/\epsilon$ is a short timescale associated with short wave-like disturbances of $O(\epsilon)$. Then s is a long lengthscale associated with the curving of the trajectory of the jet, while $\bar{s}$ is associated with waves with length of the order of the jet radius.

We can investigate the linear instability of the above steady solution caused by viscous perturbations (using either the leading-order or higher-order steady solution from the previous section). These linear viscous perturbations disturb the basic

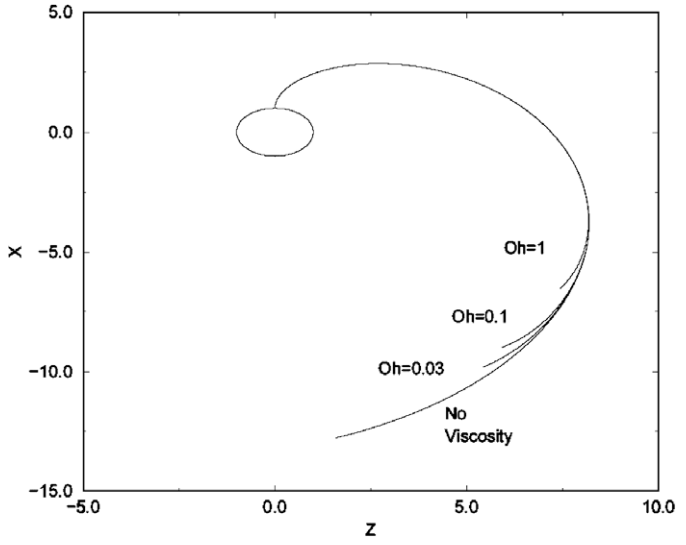

Fig. 1. Graph showing the trajectory including terms from both leading-order and next-order for various Ohnesorge numbers ($Rb=2, We=18,000$, $\epsilon=0.1$). The circle represents the container.

steady solution (denoted by a quantity with an overbar in (27)) by unsteady quantities presented with a tilde. Substituting these perturbations into our viscous equations of motion, linearising in the unsteady quantities (i.e. taking terms of $O(\delta)$), and taking the leading-order equations in ϵ, we obtain

$$n\frac{\partial\tilde{u}}{\partial\bar{s}}+\tilde{v}+n\frac{\partial\tilde{v}}{\partial n}+\frac{\partial\tilde{w}}{\partial\phi}=0, \tag{28}$$

$$\frac{\partial\tilde{u}}{\partial\bar{t}}+u_0(s)\frac{\partial\tilde{u}}{\partial\bar{s}}=-\frac{\partial\tilde{p}}{\partial\bar{s}}+\frac{Oh}{We^{1/2}}\left(\frac{\partial^2\tilde{u}}{\partial\bar{s}^2}+\frac{1}{n}\frac{\partial\tilde{u}}{\partial n}+\frac{\partial^2\tilde{u}}{\partial n^2}+\frac{1}{n^2}\frac{\partial^2\tilde{u}}{\partial\phi^2}\right), \tag{29}$$

$$\begin{aligned}&\frac{\partial\tilde{v}}{\partial\bar{t}}+u_0(s)\frac{\partial\tilde{v}}{\partial\bar{s}}+u_0(s)\cos\phi\left(Z_s\frac{\partial^2\widetilde{X}}{\partial\bar{s}\partial\bar{t}}-X_s\frac{\partial^2\widetilde{Z}}{\partial\bar{s}\partial\bar{t}}\right)-\cos\phi\left(X_s\frac{\partial^2\widetilde{Z}}{\partial\bar{s}^2}-Z_s\frac{\partial^2\widetilde{X}}{\partial\bar{s}^2}\right)u_0^2(s)=-\frac{\partial\tilde{p}}{\partial n}\\&\quad+\frac{Oh}{We^{1/2}}\left(-u_0\cos\phi\left(X_s\frac{\partial^3\widetilde{Z}}{\partial\bar{s}^3}-Z_s\frac{\partial^3\widetilde{X}}{\partial\bar{s}^3}\right)+\frac{\partial^2\tilde{v}}{\partial\bar{s}^2}\frac{1}{n}\frac{\partial\tilde{v}}{\partial n}+\frac{\partial^2\tilde{v}}{\partial n^2}+\frac{1}{n^2}\left(-\tilde{v}+\frac{\partial^2\tilde{v}}{\partial\phi^2}-2\frac{\partial\tilde{w}}{\partial\phi}\right)\right),\end{aligned} \tag{30}$$

$$\begin{aligned}&\frac{\partial\tilde{w}}{\partial\bar{t}}+u_0(s)\frac{\partial\tilde{w}}{\partial\bar{s}}+u_0(s)\sin\phi\left(X_s\frac{\partial^2\widetilde{Z}}{\partial\bar{s}\partial\bar{t}}-Z_s\frac{\partial^2\widetilde{X}}{\partial\bar{s}\partial\bar{t}}\right)+\sin\phi\left(X_s\frac{\partial^2\widetilde{Z}}{\partial\bar{s}^2}-Z_s\frac{\partial^2\widetilde{X}}{\partial\bar{s}^2}\right)u_0^2(s)=-\frac{1}{n}\frac{\partial\tilde{p}}{\partial\phi}\\&\quad+\frac{Oh}{We^{1/2}}\left(u_0\sin\phi\left(X_s\frac{\partial^3\widetilde{Z}}{\partial\bar{s}^3}-Z_s\frac{\partial^3\widetilde{X}}{\partial\bar{s}^3}\right)+\frac{\partial^2\tilde{w}}{\partial\bar{s}^2}\frac{1}{n}\frac{\partial\tilde{w}}{\partial n}+\frac{\partial^2\tilde{w}}{\partial n^2}+\frac{1}{n^2}\left(-\tilde{w}+\frac{\partial^2\tilde{w}}{\partial\phi^2}+2\frac{\partial\tilde{v}}{\partial\phi}\right)\right),\end{aligned} \tag{31}$$

$$\frac{\partial\widetilde{R}}{\partial\bar{t}}+\left(Z_s\frac{\partial\widetilde{X}}{\partial\bar{t}}-X_s\frac{\partial\widetilde{Z}}{\partial\bar{t}}\right)\cos\phi-\tilde{v}+u_0(s)\frac{\partial\widetilde{R}}{\partial\bar{s}}=0\quad\text{on } n=R_0, \tag{32}$$

$$\frac{\partial\tilde{v}}{\partial\bar{s}}+\frac{\partial\tilde{u}}{\partial n}-u_0\cos\phi\left(X_s\frac{\partial^2\widetilde{Z}}{\partial\bar{s}^2}-Z_s\frac{\partial^2\widetilde{X}}{\partial\bar{s}^2}\right)=0\quad\text{on } n=R_0, \tag{33}$$

$$\tilde{p}-\frac{2Oh}{We^{1/2}}\frac{\partial\tilde{v}}{\partial n}=\frac{1}{We}\left(-\frac{1}{R_0^2}\left(\widetilde{R}+\frac{\partial^2\widetilde{R}}{\partial\phi^2}\right)+\cos\phi\left(X_s\frac{\partial^2\widetilde{Z}}{\partial\bar{s}^2}-Z_s\frac{\partial^2\widetilde{X}}{\partial\bar{s}^2}\right)-\frac{\partial^2\widetilde{R}}{\partial\bar{s}^2}\right)\quad\text{on } n=R_0, \tag{34}$$

$$\tilde{v}=\tilde{w}=0\quad\text{on } n=0, \tag{35}$$

$$\text{and}\quad X_s\frac{\partial\widetilde{X}}{\partial\bar{s}}+Z_s\frac{\partial\widetilde{Z}}{\partial\bar{s}}=0, \tag{36}$$

$$u_0=\left(1+\left(X^2+2X+Z^2\right)/Rb^2+2(1-1/R_0)/We\right)^{\frac{1}{2}} \tag{37}$$

is the leading-order jet speed from Wallwork et al. [1] and is the solution to (5)–(16). To investigate the higher-order steady state in the previous section, it is instead necessary to retain terms of $O(1)$ and $O(\epsilon)$ in the expansion in ϵ.

We look for solutions in modes of the form

$$\left.\begin{aligned}\tilde{\mathbf{u}}&=\hat{\mathbf{u}}(s,n,\phi,t)\exp\left(ik(s)\bar{s}+\lambda(s)\bar{t}\right)+c.c.,\\\tilde{p}&=\hat{p}(s,n,\phi,t)\exp\left(ik(s)\bar{s}+\lambda(s)\bar{t}\right)+c.c.,\\\widetilde{R}&=\widehat{R}(s,\phi,t)\exp\left(ik(s)\bar{s}+\lambda(s)\bar{t}\right)+c.c.,\\\widetilde{\mathbf{X}}&=\widehat{\mathbf{X}}(s,t)\exp\left(ik(s)\bar{s}+\lambda(s)\bar{t}\right)+c.c.,\end{aligned}\right\} \tag{38}$$

where $\hat{\mathbf{u}}=\hat{u}\mathbf{e_s}+\hat{v}\mathbf{e_n}+\hat{w}\mathbf{e}_\phi$, $\widehat{\mathbf{X}}=\widehat{X}\mathbf{i}+\widehat{Z}\mathbf{k}$. In addition *c.c.* denotes the complex conjugate, $k(s)$ is the wavenumber and $\lambda(s)$ is the wave frequency. We solve the resulting set of linear equations. Looking for solutions by expanding the remaining unknowns (in the variables with "hats") in Fourier series in ϕ, we find a countably infinite set of eigenvalue relationships, each associated with $\cos(n\phi)$ or $\sin(n\phi)$ for each integer n. After some lengthy algebra we determine that these are stable modes for $n\geqslant 1$, plus one unstable mode, corresponding to $n=0$, which has the eigenvalue relation

$$\begin{aligned}&-2ik^5OhWeI_1(\tilde{k}R_0)I_0(kR_0)R_0^2u_0+k^5I_1(kR_0)\sqrt{We}I_1(\tilde{k}R_0)R_0^2+k^4I_0(kR_0)We^{3/2}R_0^2I_1(\tilde{k}R_0)u_0^2\\&\quad-2ik^4OhWeI_1(\tilde{k}R_0)I_1(kR_0)R_0u_0-2k^4OhWeI_1(\tilde{k}R_0)I_0(kR_0)R_0^2\lambda+4ik^4OhWeI_1(kR_0)I_0(\tilde{k}R_0)\tilde{k}R_0^2u_0\\&\quad+4k^3OhWeI_1(kR_0)I_0(\tilde{k}R_0)\tilde{k}R_0^2\lambda-2ik^3OhWeI_1(\tilde{k}R_0)I_0(kR_0)R_0^2\tilde{k}^2u_0-I_1(kR_0)k^3\sqrt{We}I_1(\tilde{k}R_0)\\&\quad-2ik^3I_0(kR_0)We^{3/2}R_0^2I_1(\tilde{k}R_0)\lambda-2k^3OhWeI_1(\tilde{k}R_0)I_1(kR_0)R_0\lambda-k^3\tilde{k}^2I_1(kR_0)\sqrt{We}I_1(\tilde{k}R_0)R_0^2\\&\quad-2k^2OhWeI_1(\tilde{k}R_0)I_0(kR_0)R_0^2\tilde{k}^2\lambda+k^2I_0(kR_0)We^{3/2}R_0^2I_1(\tilde{k}R_0)u_0^2\tilde{k}^2-k^2I_0(kR_0)We^{3/2}R_0^2I_1(\tilde{k}R_0)\lambda^2\\&\quad+2ik^2\tilde{k}^2OhWeI_1(\tilde{k}R_0)I_1(kR_0)R_0u_0-2ikI_0(kR_0)We^{3/2}R_0^2I_1(\tilde{k}R_0)u_0\tilde{k}^2\lambda+I_1(kR_0)k\sqrt{We}I_1(\tilde{k}R_0)\tilde{k}^2\\&\quad+2k\tilde{k}^2OhWeI_1(\tilde{k}R_0)I_1(kR_0)R_0\lambda-I_0(kR_0)We^{3/2}R_0^2I_1(\tilde{k}R_0)\lambda^2\tilde{k}^2=0,\end{aligned} \tag{39}$$

where

$$\tilde{k} = \sqrt{k^2 + \frac{\sqrt{We}(\lambda + iku_0)}{Oh}} \tag{40}$$

and I_n is the modified Bessel function of order n. Note for this mode $\tilde{w} = 0$. If $R_0 = u_0 = 1$ then this reduces to the eigenvalue relationship for a straight viscous jet. However, in this paper R_0 and u_0 are functions of arclength s, and depend upon the rotation parameter Rb and satisfy the differential equations (5)–(16).

This eigenvalue relationship can be considered in two different ways, temporal instability or spatial instability.

4.1. Temporal instability

Temporal instability corresponds to k real and (39) is an algebraic equation to be solved for λ, which will be complex, describing the temporal growth rate $Re(\lambda)$ of the wave and its frequency $Im(\lambda)$. Instability here occurs for $Re(\lambda) > 0$.

In the case of temporal instability it is necessary to determine the most unstable wavenumber $k = k^*(s)$ for which the growth rate of the mode $Re(\lambda)$ is a maximum for each value of the arclength s. In this way, the growth rate, frequency and the wavelength of the most unstable mode will vary down the jet.

Taking $Oh = 0$ in the dispersion relation (39), we obtain

$$k^* = \frac{0.697}{R_0(s)} \tag{41}$$

and

$$\lambda_0 = -ik^* u_0(s) + \sqrt{\frac{k^* I_1(k^* R_0(s))}{We I_0(k^* R_0(s))}\left(\frac{1}{R_0^2(s)} - k^{*2}\right)}, \tag{42}$$

where $R_0(s)$ and $u_0(s)$ satisfy the steady equations (5)–(16). These steady equations were solved computationally in Wallwork et al. [1], and $R_0(s)$ and $u_0(s)$ were obtained numerically. Since $Re(\lambda_0) > 0$ this mode is unstable. In fact (42) gives unstable waves for all $0 < k^* < 1/R_0(s)$, though the value of k^* given by (41) makes $Re(\lambda_0)$ a maximum. This temporal instability result is the inviscid result of Wallwork et al. [1].

Taking the long wavelength limit, $k \to 0$, of the eigenvalue relationship (39) for $Oh = O(1)$ and writing

$$\lambda = -iku_0(s) + \hat{\lambda} \tag{43}$$

gives

$$\hat{\lambda} \sim k\frac{-6R_0(s)Ohk + 2\sqrt{9R_0^2(s)Oh^2k^2 - 2R_0^3(s)k^2 + 2R_0(s)}}{4\sqrt{We}R_0(s)}. \tag{44}$$

Examining the most unstable mode from this above long wavelength result gives

$$k^* = \frac{1}{2^{1/4}R_0^{3/4}(s)\sqrt{\sqrt{2R_0(s)} + 3Oh}}. \tag{45}$$

Substituting this result for k^* into the above result for $\hat{\lambda}$ shows that this long wavelength mode is always unstable.

Also we can see that taking $Oh = 0$ in the long wavelength result (45) gives

$$k^* = \frac{1}{\sqrt{2}R_0(s)} \approx \frac{0.697}{R_0(s)} \tag{46}$$

and so the longwavelength approximation happens to also be a reasonable numerical approximation for the shorter inviscid waves. The above results show that an increase in viscosity causes a decrease in k^* and hence an increase in the wavelength of the most unstable mode. Also, the temporal growth rate of this mode decreases with an increase in viscosity, as would be expected. All of the above results correspond to results for straight liquid jets, with the important exception that R_0 is a constant for a uniform straight liquid jet [8], whereas here it is a function of s.

Rotation enters the above formulation via $R_0(s)$ and $u_0(s)$ which are dependent upon Rb, and the mode varies with the long lengthscale s. Since $u_0(s)$ increases with s and $R_0(s)$ decreases with s for the curved jet arising in this rotational problem (the jet is accelerating: see Wallwork et al. [1]), we see that the wavelength of the most unstable mode $2\pi/k^*$ decreases as s increases, whilst the growth rate $Re(\lambda)$, the wave frequency $-Im(\lambda)$ and the wave speed $-Im(\lambda)/k^*$ all increase with s.

Since the rotation of the container, given by Rb, does not appear explicitly in the above expressions for instability, but appears instead in the formulae governing $u_0(s)$ and $R_0(s)$, it is instructive to consider these results in terms of small s asymptotics. We solve the leading-order steady equations (5)–(16) by posing algebraic expansions in s, and substitute these into the instability results giving

$$k^* \sim \frac{1}{\sqrt{2+3\sqrt{2}Oh}}\left(1+\frac{sWe}{4Rb^2(2We+1)}\left(3+\frac{\sqrt{2}}{\sqrt{2}+3Oh}\right)\right) \tag{47}$$

for long waves as $s \to 0$. Consequently, for small s at least, increasing the rotation rate of the container (i.e. decreasing Rb) increases the wavenumber and the growth rate of the most unstable mode.

We can determine numerically the wavenumber $k = k^*$ which gives the most unstable mode for each s by solving (39) directly. Figs. 2 and 3 show the growth rate of this most unstable mode and k^* plotted against s for various Ohnesorge numbers. The trends can be seen to agree with the above conclusions from the asymptotics. Figs. 4 and 5 show the growth rate $Re(\lambda)$ and the most unstable wavenumber k^* plotted against s for various values of Rb. Again the trends predicted from the asymptotics can be observed.

4.2. Spatial instability

For spatial instability $\lambda = -i\omega$ where ω is a real frequency. This was developed in Keller et al. [9] and shown to be physically more realistic than the temporal instability. The eigenvalue relationship (39) is then solved for k which will be com-

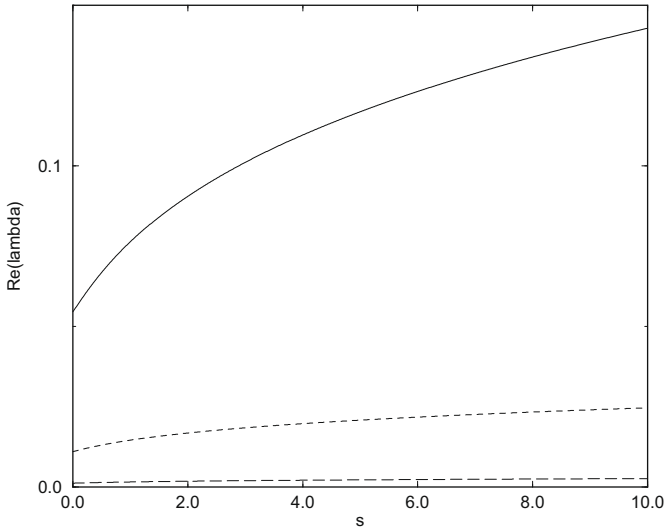

Fig. 2. Graph showing the growth rate $Re(\lambda_0)$ of the most unstable mode against arclength s for various Ohnesorge numbers. The solid curve shows $Oh = 0.365$, the short-dashed curve below that shows $Oh = 3.65$ and the long-dashed curve below that shows $Oh = 36.52$. ($We = 13.33, Rb = 1.12$).

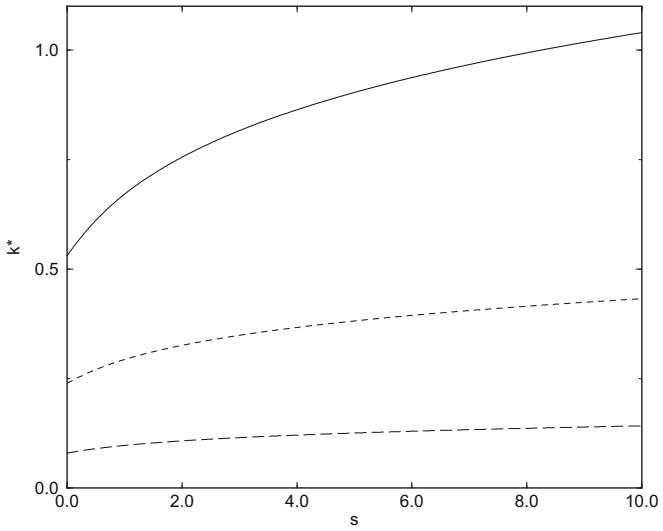

Fig. 3. Graph showing the wavenumber of the most unstable mode k^* against arclength s for various Ohnesorge numbers. The solid curve shows $Oh = 0.365$, the short-dashed curve below that shows $Oh = 3.65$ and the long-dashed curve below that shows $Oh = 36.52$. ($We = 13.33, Rb = 1.12$).

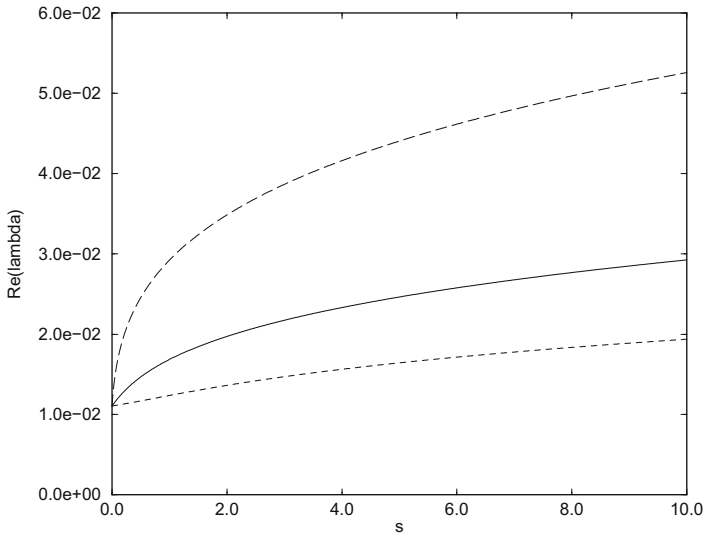

Fig. 4. Graph showing the growth rate $Re(\lambda_0)$ of the most unstable mode against arclength s for various values of Rb. The solid curve shows $Rb = 0.749$, the short-dashed curve below that shows $Rb = 2.25$ and the long-dashed curve at the top shows $Rb = 0.225$. $(We = 13.33, Oh = 3.65)$.

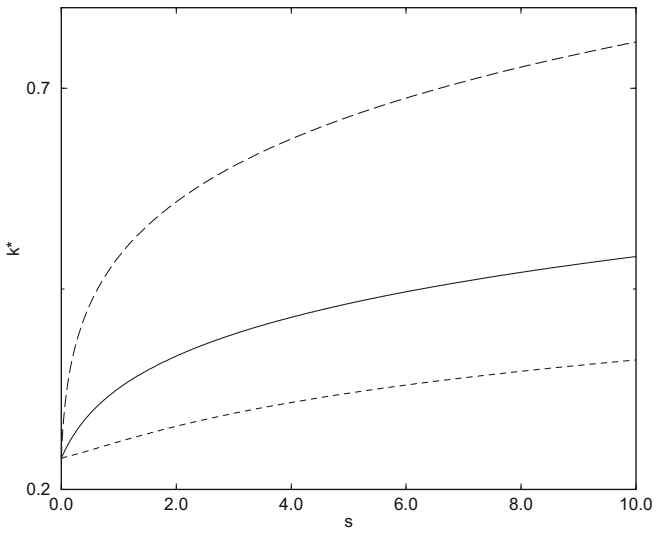

Fig. 5. Graph showing the wavenumber of the most unstable mode k^* against arclength s for various values of Rb. The solid curve shows $Rb = 0.749$, the short-dashed curve below that shows $Rb = 2.25$ and the long-dashed curve at the top shows $Rb = 0.225$. $(We = 13.33, Oh = 3.65)$.

plex, describing the wavenumber of the wave $Re(k)$ and its spatial growth rate $-Im(k)$. In this case, instability occurs when $Im(k) < 0$.

Comparing a longwave analysis for temporal and spatial instability, we write $k = \omega/u_0 + iK$, solving the eigenvalue relationship for K in the limit $\omega \to 0$. Looking for the frequency of the most unstable mode $\omega = \omega^*$ which, after some algebra, gives

$$\omega^* = u_0 k^*, \tag{48}$$

where k^* is given by (45).

The eigenvalue relationship (39) can be solved computationally. Fig. 6 shows the frequency ω of the most unstable mode plotted against s for various Ohnesorge numbers, with decreasing Ohnesorge number corresponding to increasing ω. Figs. 7 and 8 show numerical solutions to (39) at two different values of the arclength s. Each line on these graphs has been constructed by varying ω from 0 to ∞. On each line ω is real. The figures describe two different points on the same jet, and the most unstable mode on each curve occurs at the minimum value. Figs. 7 and 8 show that increasing the Ohnesorge number causes the jet to be less unstable since the waves are more heavily damped by viscosity. For larger values of viscosity the

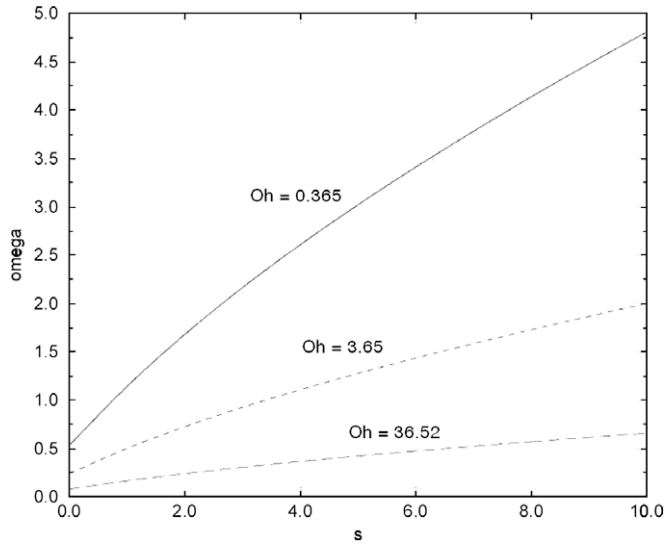

Fig. 6. Graph showing the frequency of the most unstable mode ω against arclength s for various Ohnesorge numbers. The solid curve shows $Oh = 0.365$, the short-dashed curve below shows $Oh = 3.65$ and the long-dashed curve below that shows $Oh = 36.52$. ($We = 13.33, Rb = 1.12$).

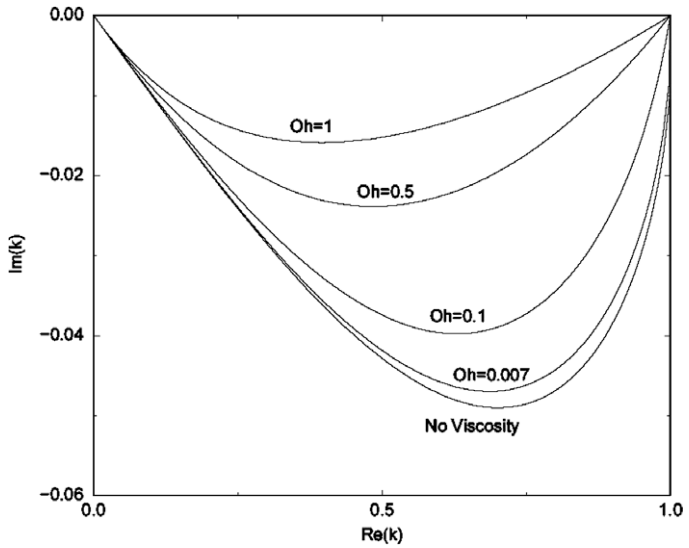

Fig. 7. Graph showing numerically $Im(k)$ against $Re(k)$ at $s = 0$ for various Ohnesorge numbers ($We = 18,000, Rb = 2$). The frequency ω is real on each line, but varies from 0 to ∞ along each line from left to right.

most unstable mode occurs at longer wavelengths, i.e. at smaller values of $Re(k)$. These trends for spatial instability all agree with those of temporal instability. However, the numerical result for the most unstable mode differ between the temporal and spatial instability cases, and Keller et al. [9] has shown that the spatial instability approach is most physically realistic.

5. Break-up length, droplet size and satellite drop formation

We now determine the effect of viscosity on the break-up length of the jet. The leading-order steady free-surface amplitude is $R_0(s)$. The unsteady wave-like perturbation to this is denoted by $\widetilde{R}(s, \bar{s}, t, \bar{t}, \phi)$. If the amplitude of this unsteady disturbance at the orifice (at $s = 0$) is δ then we have the leading-order condition for jet break-up from linear spatial instability theory as

$$1 = -\delta \frac{\omega^*(s)}{2u_0^2(s) Im(k(s))} \exp\left(-\frac{s Im(k(s))}{\epsilon}\right). \tag{49}$$

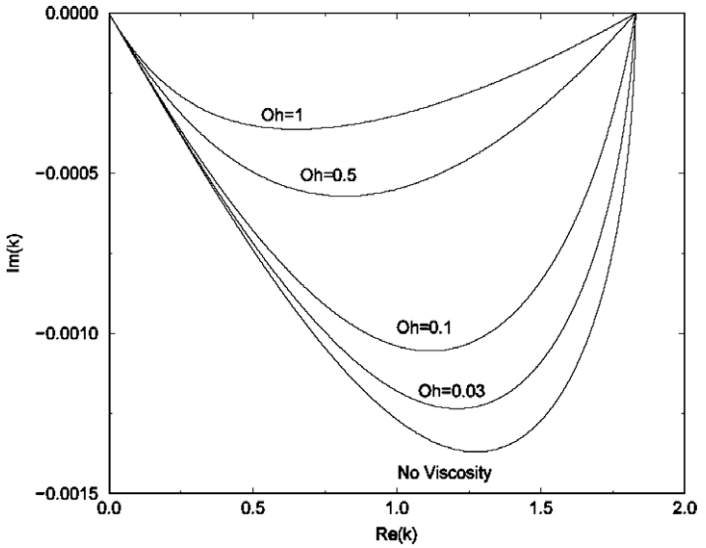

Fig. 8. Graph showing numerically $Im(k)$ against $Re(k)$ at $s = 15$ for various Ohnesorge numbers ($We = 18,000, Rb = 2$). The frequency ω is real on each line, but varies from 0 to ∞ along each line from left to right.

It is necessary that the perturbation at the orifice be sufficiently small that this condition is not satisfied at $s = 0$, which means that

$$2^{1/4} \gg \delta\sqrt{3OhWe}. \tag{50}$$

Eq. (49) can be solved numerically to determine the relationship between the break-up length of the jet and the rotation rate parameter *Rb* for various values of the viscosity parameter *Oh*. This is shown in Fig. 9. Note that the curve is not monotonic for the smallest Ohnesorge number. That is, increasing the rotation rate of the container (i.e. decreasing *Rb*) may increase or decrease the break-up length of the jet, whilst holding all other parameters constant. This requires some explanation. The results from the previous section show that increasing the rotation rate of the container increases the wave speed of the disturbances but also increases the growth rate of those disturbances. These two effects are in competition to make the jet either longer or shorter, respectively, and therefore no simple monotonic relationship necessarily exists between break-up length and rotation rate.

It is now also possible to determine the wavelength of the disturbance at the predicted point of break-up. Fig. 10 shows this wavelength plotted against *Rb* for various *Oh*. From this it is possible to determine the main droplet size produced by this

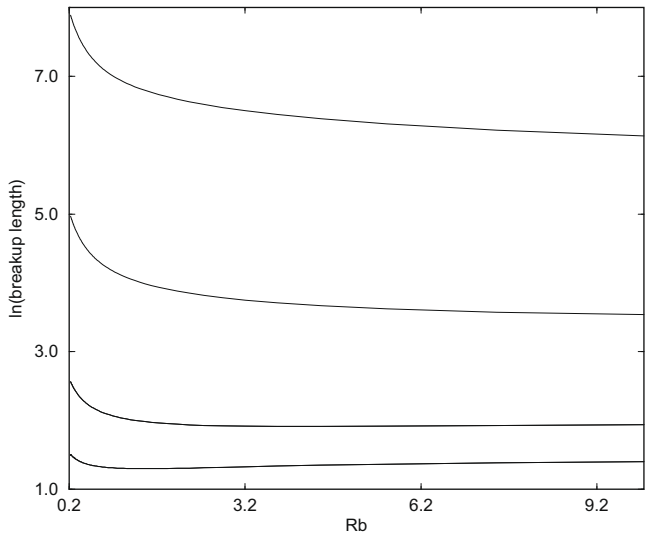

Fig. 9. The natural logarithm of the break-up length plotted against *Rb* for various Ohnesorge numbers. The curves show from top to bottom: $Oh = 36.5$, $Oh = 3.65$, $Oh = 0.365$ and $Oh = 0.00365$. ($We = 13.33, \epsilon = 0.0235, \delta = 10^{-8}$).

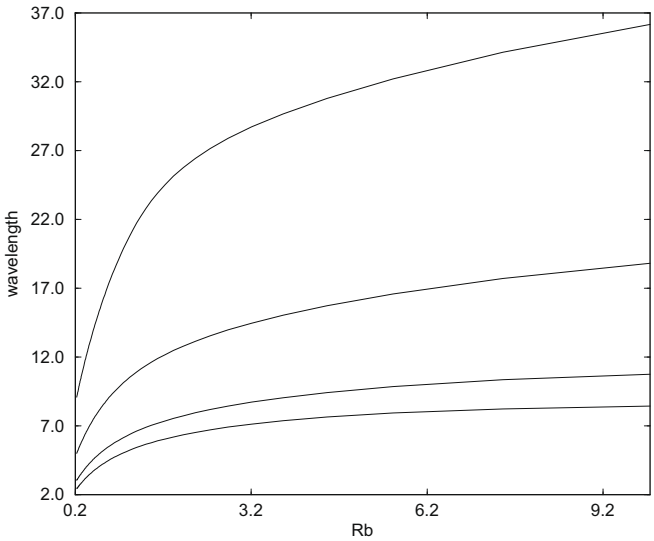

Fig. 10. The wavelength of the most unstable mode at the point of break-up plotted against *Rb* for various Ohnesorge numbers. The curves show from top to bottom: $Oh = 36.5$, $Oh = 3.65$, $Oh = 0.365$ and $Oh = 0.00365$. ($We = 13.33, \epsilon = 0.0235, \delta = 10^{-8}$).

instability by calculating the volume of the liquid over one wavelength of the jet instability at the break-up point. Since the droplets will be approximately spherical, the droplet radius can be determined from this volume. Fig. 11 shows this non-dimensional radius (with respect to the size of the orifice a) plotted against *Oh* for various *Rb*. Note that the relationship between the droplet radius is not monotonic with *Oh*. This also requires some explanation. As the Ohnesgorge number is increased, while holding all other parameters constant, the wavelength of the unstable mode at instability increases (Fig. 3). However, since the break-up length also increases (Fig. 9) and the jet radius $R_0(s)$ thins along the jet due to jet acceleration, the maximum radius of the unstable wave at the break-up point decreases with increasing Ohnesgorge number. Hence increasing viscosity makes the unstable waves at the break-up point longer but with smaller amplitude. Hence these two competing mechanisms are producing counter-influences on the size of the droplets produced by instability, and make it possible for the droplet size to increase or decrease with increasing viscosity (Fig. 11). Fig. 12 shows droplet radius plotted against *Oh*.

The extent of satellite drop formation can be estimated by considering the range of unstable wavenumbers. Section 4 shows that travelling waves are unstable for $0 < k < 1/R_0(s)$ for both temporal and spatial instability. Thus as $1/R_0(s)$

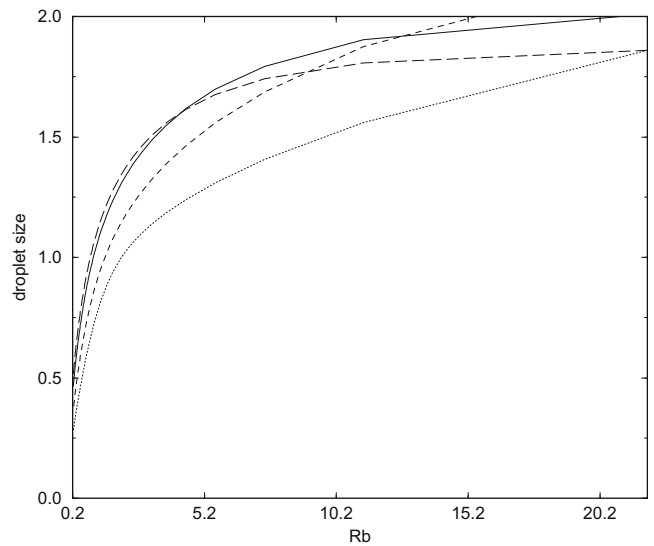

Fig. 11. The droplet radius produced by instability plotted against *Rb* for various *Oh*. The long-dashed curve shows $Oh = 0.00365$, the solid curve shows $Oh = 0.365$, the short-dashed curve shows $Oh = 3.65$ and the dotted curve underneath the other curves shows $Oh = 36.5$. ($We = 13.33, \epsilon = 0.0235$, $\delta = 10^{-8}$).

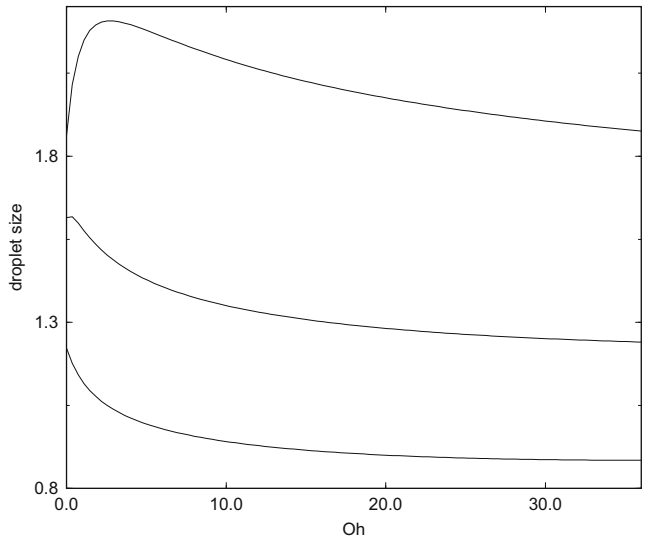

Fig. 12. The droplet radius produced by instability plotted against *Oh* for various *Rb*. The curves show from top to bottom: $Rb = 22.47$, $Rb = 4.49$ and $Rb = 1.50$. ($We = 13.33, \epsilon = 0.0235, \delta = 10^{-8}$).

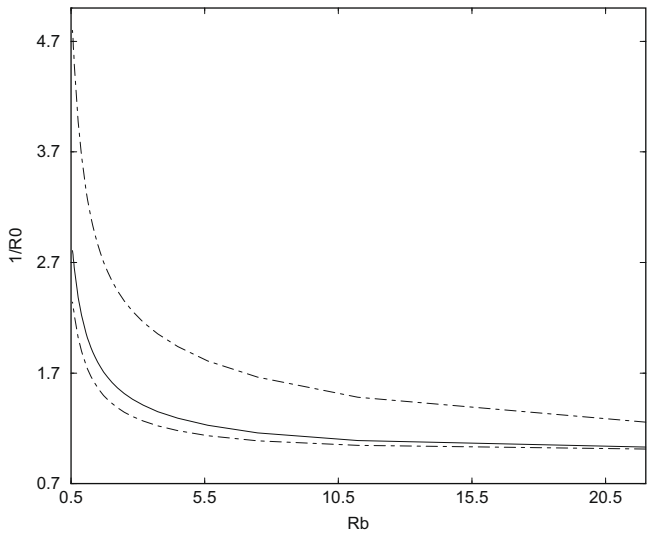

Fig. 13. The upper limit of unstable wavenumbers $1/R_0$ at the break-up point plotted against *Rb* for various *Oh*. The upper curve shows $Oh = 3.65$, the middle curve shows $Oh = 0.365$ and the lower curve shows $Oh = 0.0365$. ($We = 13.33$ and $\epsilon = 0.02$).

increases along the jet, shorter waves become unstable, which could produce satellite drops. Fig. 13 shows $1/R_0(s)$ at the break-up point on the jet plotted against *Rb* for various values of *Oh*. Satellite drop formation is a non-linear process, but we suggest that the availability of these short unstable modes will increase the frequency of satellites. We present some experimental evidence to support this claim in Section 7.

6. Linear instability of the steady state solutions: Long waves

We now examine long travelling wave disturbances of the steady state by posing the expansions

$$\left.\begin{aligned} \mathbf{u} &= \bar{\mathbf{u}}(s,n,\phi,\epsilon) + \delta\tilde{\mathbf{u}}(s,n,\phi,t),\\ R &= \overline{R}(s,\phi,\epsilon) + \delta\widetilde{R}(s,\phi,t),\\ p &= \bar{p}(s,n,\phi,\epsilon) + \delta\tilde{p}(s,n,\phi,t),\\ \mathbf{X} &= \overline{\mathbf{X}}(s,\epsilon) + \delta\widetilde{\mathbf{X}}(s,t), \end{aligned}\right\} \tag{51}$$

where the variables with bars are the steady solutions and the variables with a tilde correspond to an unsteady perturbation, which aside from the fact that these perturbations do not depend upon $\bar{s}$ or $\bar{t}$, are similar to (27). Determining equations at $O(\delta)$, examining the leading-order behaviour in ϵ, and eliminating $\tilde{v}, \tilde{w}$ and $\tilde{p}$, we find

$$\tilde{u}_t + (\tilde{u}u_0)_s + 2u_0(X_sZ_{ss} - X_{ss}Z_s)\left(\widetilde{X}_tZ_s - \widetilde{Z}_tX_s\right) = -\frac{\tilde{\kappa}_s}{We} + \frac{2}{Rb}\left(\widetilde{X}_tZ_s - \widetilde{Z}_tX_s\right) + \frac{(X+1)\widetilde{X}_s + \widetilde{X}X_s + \left(Z\widetilde{Z}\right)_s}{Rb^2} + \frac{3}{\widetilde{Re}}\left(\tilde{u}_{ss} + \left((X_sZ_{ss} - X_{ss}Z_s)\left(\widetilde{X}_tZ_s - \widetilde{Z}_tX_s\right)\right)_s + 2\frac{R_{0_s}}{R_0}\left(\tilde{u}_s + (X_sZ_{ss} - X_{ss}Z_s)\left(\widetilde{X}_tZ_s - \widetilde{Z}_tX_s\right)\right) + 2\frac{\widetilde{R}_su_{0_s}}{R_0} - 2\frac{u_{0_s}R_{0_s}\widetilde{R}}{R_0^2}\right), \tag{52}$$

$$\widetilde{R}_t + \frac{1}{2}\left(u_{0_s}\widetilde{R} + R_0\tilde{u}_s\right) + \frac{1}{2}R_0(X_sZ_{ss} - X_{ss}Z_s)\left(\widetilde{X}_tZ_s - \widetilde{Z}_tX_s\right) + \tilde{u}R_{0_s} + u_0\widetilde{R}_s - R_{0_s}\left(\widetilde{X}_tX_s + \widetilde{Z}_tZ_s\right) = 0, \tag{53}$$

$$\left(\widetilde{X}_tZ_s - \widetilde{Z}_tX_s\right)_t + u_0\left(\widetilde{X}_{st}Z_s - \widetilde{Z}_{st}X_s\right) + u_0\left(\widetilde{X}_tZ_s - \widetilde{Z}_tX_s\right)_s - \frac{1}{2}u_{0_s}\left(\widetilde{X}_tZ_s - \widetilde{Z}_tX_s\right) + \frac{3}{\widetilde{Re}}(X_sZ_{ss} - X_{ss}Z_s)^2\left(\widetilde{X}_tZ_s - \widetilde{Z}_tX_s\right) = 2u_0\tilde{u}(X_sZ_{ss} - X_{ss}Z_s) + u_0^2\left(X_s\widetilde{Z}_{ss} + \widetilde{X}_sZ_{ss} - \widetilde{X}_{ss}Z_s - X_{ss}\widetilde{Z}_s\right) - \frac{2\tilde{u}}{Rb} + \frac{(X+1)\widetilde{Z}_s + \widetilde{X}Z_s - \widetilde{Z}X_s - Z\widetilde{X}_s}{Rb^2} - \frac{3}{\widetilde{Re}}\left(\tilde{u}_s(X_sZ_{ss} - X_{ss}Z_s) + u_{0_s}\left(X_s\widetilde{Z}_{ss} + \widetilde{X}_sZ_{ss} - \widetilde{X}_{ss}Z_s - X_{ss}\widetilde{Z}_s\right)\right) + \frac{X_sZ_{ss} - X_{ss}Z_s}{WeR_0^2}\widetilde{R} - \frac{X_s\widetilde{Z}_{ss} + \widetilde{X}_sZ_{ss} - \widetilde{X}_{ss}Z_s - X_{ss}\widetilde{Z}_s}{WeR_0} \tag{54}$$

and

$$X_s\widetilde{X}_s + Z_s\widetilde{Z}_s = 0, \tag{55}$$

where $\tilde{\kappa}$ is the mean curvature of the free-surface, namely

$$\tilde{\kappa} = -\frac{\widetilde{R}}{R_0^2} + \epsilon^2\left(\widetilde{R}\frac{R_{0_s}^2}{2R_0^2} - \frac{R_{0_s}\widetilde{R}_s}{R_0} - \widetilde{R}_{ss}\right) + O(\epsilon^2) \tag{56}$$

and $\widetilde{Re} = \rho U s_0/\mu = \sqrt{We}/(\epsilon Oh)$ is the Reynolds number. Looking for wave-like disturbances

$$\begin{aligned}
\tilde{u} &= a(s,t)\exp\left(ik(s)\frac{s}{\Delta} + \lambda(s)\frac{t}{\Delta}\right),\\
\widetilde{R} &= b(s,t)\exp\left(ik(s)\frac{s}{\Delta} + \lambda(s)\frac{t}{\Delta}\right),\\
\widetilde{X} &= c(s,t)\Delta^m\exp\left(ik(s)\frac{s}{\Delta} + \lambda(s)\frac{t}{\Delta}\right),\\
\widetilde{Z} &= d(s,t)\Delta^m\exp\left(ik(s)\frac{s}{\Delta} + \lambda(s)\frac{t}{\Delta}\right),
\end{aligned} \tag{57}$$

where Δ is some constant and m is chosen to give the correct amplitude of disturbance of the unsteady perturbation, the above equations can be solved to find equations linking a, b, c and d. If Δ is considered to be large or small, then an eigenvalue relationship can be found linking k and λ. As in Eggers and Dupont [18], unstable waves are found to occur at $k = \infty$ unless both components of curvature appear at leading-order in the formulation, i.e. unless higher-order terms in ϵ are retained in $\tilde{\kappa}$. If Δ is chosen to be equal to ϵ then we effectively reintroduce $\bar{s}$ and $\bar{t}$ into these equations, corresponding to the examination of short waves in the long wavelength equations. (Whereas in Section 4 we considered short waves on the $\bar{s}$ length-scale and then found the long wave limit of those equations to be a useful approximation, this rescaling would correspond to

Table 1
A comparison between experimental and theoretical data for drop sizes (ds) for 13 different experiments.

Oh	*We*	*Rb*	ϵ	ds (theory)	ds (expt)	Sat. freq.	Sat. size	Mode
0.0036	5	0.98	0.024	1.78	1.5	0.0	–	1
0.0036	5	1.81	0.024	1.99	2.0	0.0	–	1
0.0036	5	3.53	0.024	2.10	2.5	0.0	–	1
0.0029	17.5	1.07	0.024	1.68	1.6	0.4	0.4	2
0.0029	17.5	2.01	0.024	1.93	2.1	1.0	0.6	2
0.0029	17.5	3.94	0.024	2.08	2.1	0.7	0.6	2
0.038	25	1.17	0.024	1.69	1.4	1.4	0.7	3
0.038	25	2.20	0.024	1.95	1.7	0.5	0.5	3
0.038	25	4.31	0.024	2.10	1.8	1.4	0.8	3
0.178	17.5	0.62	0.071	1.06	1.1	1.1	0.6	3
0.178	17.5	0.67	0.071	1.10	1.2	1.2	0.6	3
0.352	1.5	0.26	0.024	1.19	1.2	0.7	0.8	4
0.352	1.5	0.37	0.024	1.44	1.2	0.6	0.8	4

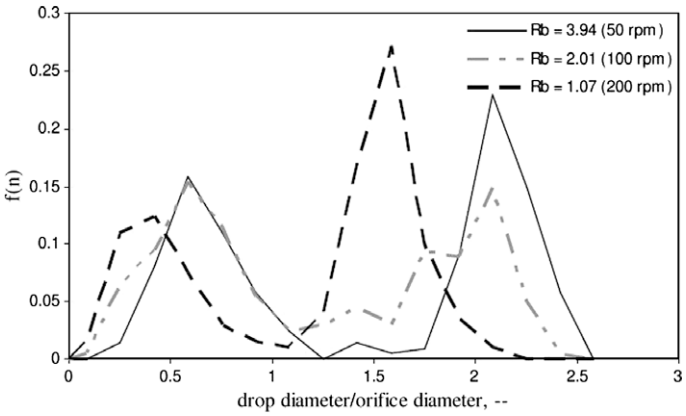

Fig. 14. Drop size distributions for three rotational rates, $Rb = 3.94$, 2.01 and 1.07 (50, 100 and 200 rpm) in break-up mode 2 ($15 < We < 20; Oh = 0.0029$).

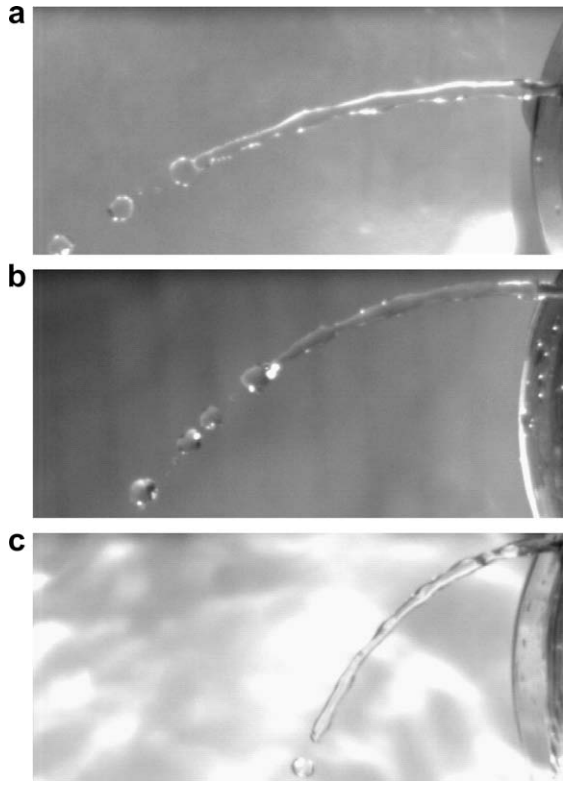

Fig. 15. Pictures of a jet emerging from the 2 mm orifice with the can rotating at different rotation rates.

taking long wave equations but then taking the short wavelength limit of those equations.) This of course should lead to the same results as in Section 4. This is indeed the case, and the eigenvalues in Section 4 as $k \to 0$ are re-obtained when this distinguished limit is taken.

However, these equations reveal an additional neutrally stable mode with frequency[1]

$$k\left(u_0(s) \pm \frac{1}{\sqrt{WeR_0(s)}}\right). \tag{58}$$

[1] Regardless of whether the above distinguished limit in Δ is taken or not. In fact we find both the unstable modes of Section 4 plus this neutral mode if $m = 2$.

These neutrally stable modes correspond to disturbances in the trajectory $\widetilde{X}$ and $\widetilde{Z}$ and appear out of Eqs. (54) and (55). If $c = d = 0$ then these modes do not exist. These modes will cause a long wave to travel along the trajectory of the jet, transforming the jet's centre line in a sinusoidal manner. Since $u_0 \to \infty$ and $R_0 \to 0$ as $s \to \infty$ these frequencies tend to infinity as $s \to \infty$. Also, note that since the frequency of the most unstable mode from Section 4 is ku_0, we see that one of the above frequencies is larger and the other smaller than this most unstable frequency.

Since the wavespeed of a linear travelling wave with frequency ω is ω/k, we can see that the most unstable mode travels at the mean streamwise speed of the steady state u_0, while one of these neutrally stable modes travels faster and the other travels slower than u_0. Moreover, the neutrally stable mode associated with the negative alternative sign in the above equation can have a negative frequency and hence travel upstream rather than downstream. Since $u_0 = R_0 = 1$ at $s = 0$ at the orifice, we can see that these waves may only travel upstream if $We < 1$.

We also notice that at high Weber numbers the above neutrally stable frequencies are approximately ku_0, and so these modes will be particularly relevant at $O(1)$ values of We and less. As these waves appear out of a long wave analysis, we might expect these waves to only be observed when the jet is sufficiently long for them to develop. Since the break-up length of the jet increases with viscosity, we then expect these modes to be particularly important for jets with high viscosity. That is we might expect these neutrally stable modes to be observed for highly viscous jets at low We. We discuss this in the following section.

Lin and Lian [19] showed that jets with $We < 1$ undergo absolute instability with waves propagating back upstream. Baird and Davidson [20] also found a discontinuity at $We = 1$, and noted that jets with $We < 1$ have more of a rounded shape than cylindrical. This was also pointed out by Keller and Weitz [21] who discovered that a jet rises instead of falls under gravity for $We < 1$. Ramos [22] also showed that a jet forms non-cylindrical shapes when $We < 1$ and that a long wavelength model

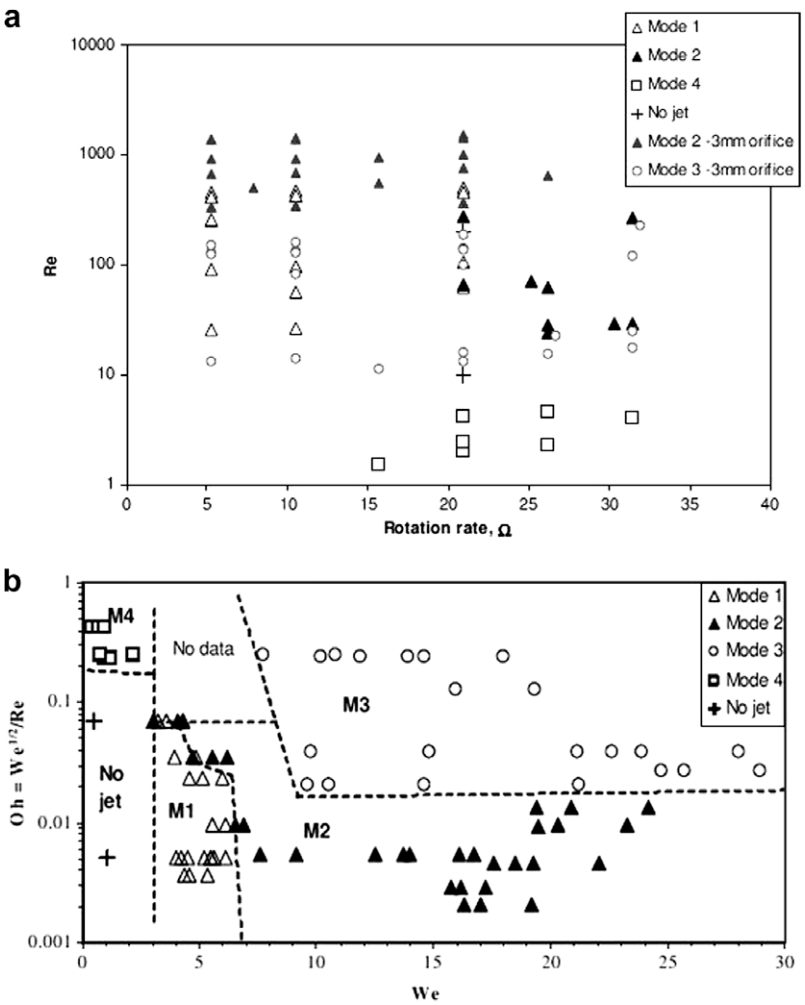

Fig. 16. Flow maps summarising the dynamics of the break-up observed in experiments. (a) Shows Reynolds Number plotted against rotation rate (radians per second). (b) Shows the same data plotted on a *Oh–We* plot. The four different types of break-up are also shown, in addition to situations where no jet was observed.

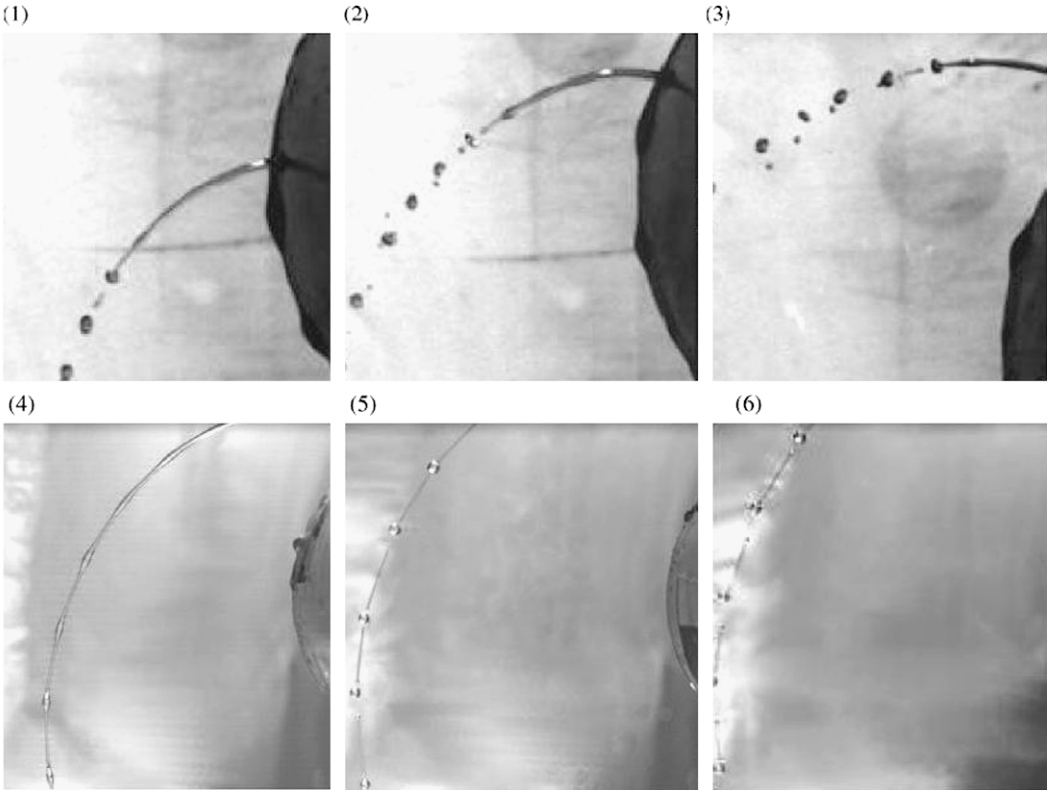

Fig. 17. Pictures of different break-up mechanisms observed in experiments. Pictures (1)–(3) show a jet at successive times with $Rb = 1.06, Oh = 0.0095$ and $We = 13.4$ We call this mode 2. Pictures (4)–(6) show a jet at successive times with $Rb = 0.80, Oh = 0.241$ and $We = 21.47$. We call this mode 3.

may not be valid for small Weber numbers. Finnicum et al. [23] identified a singularity at $We = 1$ whilst investigating two-dimensional liquid curtains falling under gravity.

7. Experiments

We briefly report experiments carried out on Newtonian liquids – specifically water and glycerol–water mixtures. (For example, a 60% glycerol and 40% water (glycerol(60)–water(40)) mixture has a viscosity approximately 10 times that of water (so $\mu \approx 0.01$ kg m^{-1} s^{-1}: see Lide [24]) with a surface tension approximately equal to 6.8×10^{-2} kg s^{-2}.) We use the same experimental apparatus as in Wallwork et al. [1] using a can of radius 4.25 cm with various different orifices between 1 mm and 3 mm in radius.

Fig. 14 shows graphs of the experimentally observed drop size distributions from three sets of experiments. Each graph shows the relative frequency of each drop size observed against the relative diameter of each droplet. (Hundreds of droplets were measured in each experiment). Note that the size distributions are bi-modal, pointing to the formation of main and satellite drops. Table 1[2] shows a summary of a comparison of drop sizes and frequencies produced from experimental drop size distributions such as Fig. 14 (see Wallwork [16] and Wong et al. [25,17] for further data) with theoretical predictions using the methods presented in earlier sections.

In these calculations we choose $\delta = 0.01$, though we did not attempt to optimise the fit between theory and experiment by selecting the appropriate value of δ. No doubt better agreement could be obtained by selecting δ but we did not want to bias the results since it is not possible to measure δ in our experiments. However, the size of the resulting droplets is only

[2] Table 1 shows a comparison between experimental and theoretical data for drop sizes for 13 different experiments. Drop size (theory) shows the size of the droplet predicted from the most unstable wavenumber at break-up. This should be compared to the experimental drop size, determined as the size of the droplet which corresponds to the maximum value on the droplet distribution curve for the main droplet (the most commonly observed main droplet). The satellite frequency column shows the relative frequency of satellites compared to main droplets observed in experiments. This is calculated as the ratio of the maximum relative frequency on the droplet distribution for the portion of that curve corresponding to satellites compared to the maximum value for the relative frequency for the main droplets. (These curves are usually bi-modal, so this is the ratio of the relative frequencies at the two maxima of the distribution.) The satellite size column shows the size of the most commonly observed satellite droplet in each experiment. The mode number in the final column refers to the dynamics of the break-up of the jet, and is assigned a number from 1 to 4 to refer to four different types of break-up. The sizes of droplets shown here are all non-dimensional relative to the size of the orifice.

weakly dependent on δ. For example, taking values of δ between 0.005 and 0.05, using (49) we predict break-up lengths between 0.164 and 0.3785 in dimensionless units for a fluid with $We = 10, Rb = 2, Oh = 0.0001$. This yields dimensionless main drop radii of between 1.7133 and 1.7797. Increasing the viscosity ($Oh = 0.1$) predicts break-up lengths between 0.197 and 0.462 and main drop radii between 1.7439 and 1.8613. Therefore, whilst break-up length is largely dependent on δ, we predict minimal differences in the main drop radii. Părău et al. [6] also showed a similar relationship for a long wavelength model. In Table 1 we can see some good areas of agreement between the experimental and theoretical predictions for the size of the main droplets (columns 5 and 6).

Fig. 15 shows the behaviour of water jets at three different rotation rates for an orifice of radius 2 mm. Fig. 16 shows several different experiments summarised on two parameter space diagrams: one diagram showing the experiments plotted for Reynolds number $Re = \sqrt{We}/Oh$ against the rotation rate Ω measured in radians per second; the second diagram shows the experiments on a Oh–We diagram. Both diagrams show the same set of experiments, with different experiments achieved by varying the water/glycerol mixture, the radius of the orifice, the rotation rate and the rotating frame exit speed U (by varying the amount of liquid inside the container). Four so-called break-up modes were identified: mode 1 where the jet produces a droplet from its end with minimal satellite formation (e.g. Fig. 15 has fairly minimal satellite formation); mode 2 where more significant satellite drop formation occurs; mode 3 where break-up appears to occur at more than one place at once; mode 4 where the jet appears to shatter behind the bifurcation point at break-up. Also there were scenarios in which no jet was obtained, and droplets were produced directly out of the orifice. Further experiments are described in Wong et al. [25,17].

Fig. 17 shows examples of what we call modes 2 and 3. Notice increased satellite drop formation in mode 2. In mode 3, a very long jet is obtained due to the high viscosity of the liquid, with a "beads-on-a-string" type structure, observed elsewhere before in other contexts (e.g. Decent and King [26] and Clasen et al. [27]). Mode 3 has long thin modes at break-up, as predicted in Section 5 for highly viscous jets. Some evidence of the cone structures observed by Peregrine et al. [28] can be observed in Fig. 17.

Fig. 18 shows an example of our so-called mode 4. Note that the jet appears to shatter behind the bifurcation point after break-up occurs. We suggest that the neutrally stable modes described in the previous section which travel upstream for small Weber numbers might be partly responsible for what is seen in Fig. 18, since information can be seen in Fig. 18 to propagate upstream after the bifurcation occurs. This agrees with the observation at the end of the previous section that the neutrally stable trajectory waves might be especially relevant for low Weber number and large viscosity since here $Oh = 0.233$

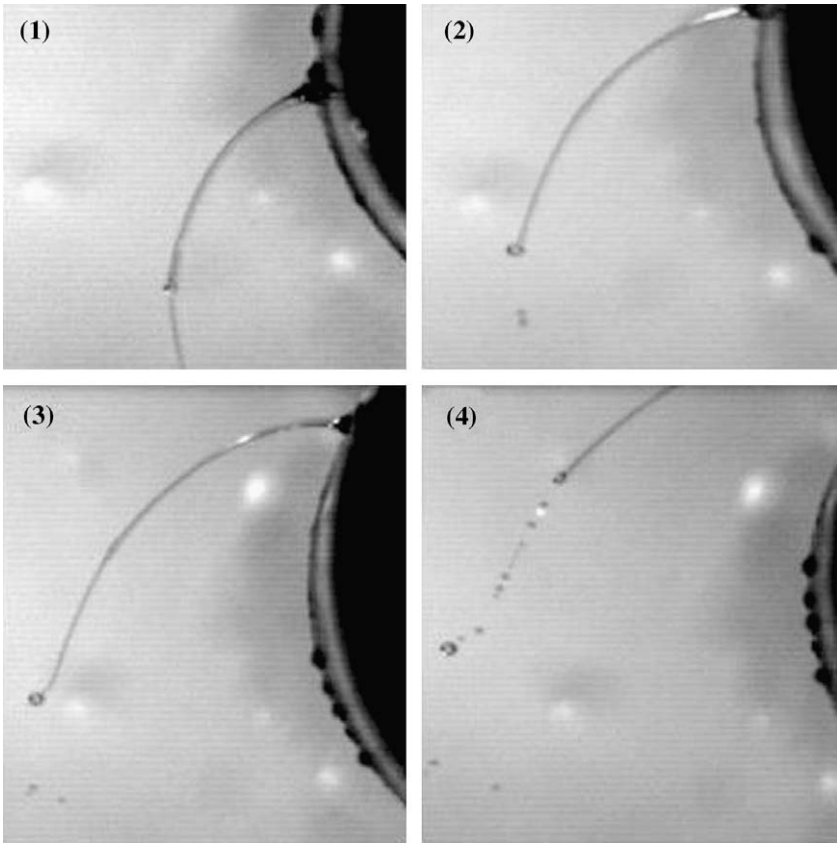

Fig. 18. Pictures (1)–(4) show experimental observations at successive time intervals for $Rb = 0.32, Oh = 0.233$ and $We = 0.9$. We call this mode 4.

(large when compared to most experimental runs) and $We = 0.9$ (small). However, break-up is clearly a non-linear event. Partridge et al. [5] and Părău et al. [6] have investigated the non-linear disturbances and show a good correlation between experimental results and theoretical predictions for break-up of a low viscosity jet.

Returning to Table 1 we observe some evidence of a general trend for satellites to become more frequent for larger values of *We*, *Oh* and rotation rates (i.e. small *Rb*). Examining Fig. 13 we see that $1/R_0(s)$ at break-up increases for increased *Oh* and increased rotation rate. From Wallwork et al. [1], we see that $1/R_0$ increases at break-up for increased Weber number (since as *We* increases, the jet speed increases, producing increased thinning). Hence it would appear that we have a general trend that as the rotation rate, *We* and *Oh* increase, $1/R_0$ increases at break-up so that shorter unstable wave modes are present at break-up, increasing the production of satellite drop formation. There is further experimental evidence for this in Fig. 16a where we see the mode with low satellite drop production (mode 1) occurring at lower rotation rate. However, of course, satellite drop formation is a non-linear process.

8. Conclusions

In summary, we have shown that the trajectory and steady state of the liquid jet emerging from a rotating container is only affected by viscosity at higher-order in ϵ. The linear instability calculation reveals similar results for both temporal and spatial instability over a wide set of parameter values. While the results are similar, they are not identical. From Keller et al. [9] it is clear that the spatial stability results are the correct ones to use. A long wavelength viscous analysis allows asymptotic formulae to be developed for these instability results. It can be seen in some cases that the temporal instability results are identical at leading-order to the spatial instability results. This is very useful to know since the temporal approach is easier to use, though less accurate. It should be noted that we may instead use the higher-order results in ϵ for the steady state in the instability calculations by replacing u_0 by $u_0 + \epsilon u_1$ and R_0 by $R_0 + \epsilon R_1$, and choosing a typical value of ϵ (such as 0.02). This enables us to determine the effects of viscosity in the steady state on the instability results.

The break-up length and mean droplet radius produced by instability can be determined using the linear instability calculations. We find that the droplet radius increases with *Rb* increasing. We also find that the break-up length of the jet does not have a monotonic relationship with *Rb*, and the droplet size does not have a monotonic relationship with *Oh*. Some good points of agreement have been obtained between theoretical and experimental measurements of the size of the drops produced by instability. The formation of satellites and break-up dynamics have been discussed in light of the theory and experiments, with some very favourable agreement.

Acknowledgement

The authors would like to thank *Norsk Hydro* and EPSRC (GR/R21349/01) for their financial support of this project.

Appendix

The leading-order problem for the trajectory of the jet described in Section 3 for a viscous jet is identical to the leading order problem for an inviscid jet presented in Wallwork et al. equations (3.18)–(3.24), namely it can be simplified using Section 3 to

$$
\begin{aligned}
p_0 &= \frac{1}{WeR_0},\\
u_0 &= \left(1 + \frac{1}{Rb^2}\left(X^2 + 2X + Z^2\right) + \frac{2}{We}\left(1 - \frac{1}{R_0}\right)\right)^{\frac{1}{2}},\\
p_1 &= \frac{n}{WeR_0}\cos\phi(X_sZ_{ss} - X_{ss}Z_s) + h_1(s),\\
v_1 &= -\frac{n}{2}\frac{du_0}{ds},\\
Z_{ss} &= \frac{WeR_0X_s}{WeR_0u_0^2 - 1}\left(\frac{2u_0}{Rb} + \frac{ZX_s - (X+1)Z_s}{Rb^2}\right),\\
R_{0s} &= -\frac{WeR_0^2((X+1)X_s + ZZ_s)}{Rb^2(2WeR_0u_0^2 + 1)},\\
X_s^2 + Z_s^2 &= 1.
\end{aligned}
$$

References

[1] I.M. Wallwork, S.P. Decent, A.C. King, R.M.S.M. Schulkes, The trajectory and stability of a spiralling liquid jet. Part 1. Inviscid theory, J. Fluid Mech. 459 (2002) 43–65.
[2] K.G. Andersen, G. Yttri, Et Porsϕ Verdt, Univesitets for Laget Oslo, 1997.

[3] S.P. Decent, A.C. King, I.M. Wallwork, Free jets spun from a prilling tower, J. Eng. Math. 42 (2002) 265–282.
[4] E.I. Părău, S.P. Decent, A.C. King, Non-linear travelling waves on a spiralling liquid jet, Wave Motion 43 (2006) 599–618.
[5] L. Partidge, D.C.Y. Wong, M.J.H. Simmons, E.I. Părău, S.P. Decent, Experimental and theoretical description of the break-up of curved liquid jets in the prilling process, Chem. Eng. Res. Des. 83 (2005) 1267–1275.
[6] E.I. Părău, S.P. Decent, M.J.H. Simmons, D.C.Y. Wong, A.C. King, Non-linear viscous jets emerging from a rotating orifice, J. Eng. Math. 57 (2007) 159–179.
[7] LORD Rayleigh, On the instability of a cylinder of viscous liquid under capillary force, Philos. Mag. 34 (1892) 145.
[8] C. Weber, Zum Zerfall eines Flussigkeitsstrahles, Z. Angew. Math. Mech. 1 (1931) 136–141.
[9] J.B. Keller, S.I. Rubinow, Y.O. Tu, Spatial instability of a jet, Phys. Fluids 16 (1973) 2052–2055.
[10] E.O. Tuck, The shape of free jets of water under gravity, J. Fluid Mech. 76 (1976) 625–640.
[11] J.M. Vanden-Broeck, J.B. Keller, Jet rising and falling under gravity, J. Fluid Mech. 124 (1982) 335–345.
[12] V.M. Entov, A.L. Yarin, The dynamics of thin liquid jets in air, J. Fluid Mech. 140 (1984) 91–111.
[13] F. Dias, J.M. Vanden-Broeck, Flows emerging from a nozzle and falling under gravity, J. Fluid Mech. 213 (1990) 465–477.
[14] A.L. Yarin, Free Liquid Jets and Films: Hydrodynamics and Rheology, Longman, New York, 1993.
[15] L.J. Cummings, P.D. Howell, On the evolution of non-axisymmetric viscous fibres with surface tension, inertia and gravity, J. Fluid Mech. 389 (2001) 361–389.
[16] I.M. Wallwork, The Trajectory and Stability of a Spiralling Liquid Jet, Ph.D. Thesis, University of Birmingham, 2002.
[17] D.C.Y. Wong, M.J.H. Simmons, S.P. Decent, E.I. Părău, A.C. King, Break-up dynamics and drop size distributions created from curved liquid jets, Int. J. Multiphase Flow 30 (2004) 499–520.
[18] J. Eggers, T.F. Dupont, Drop formation in a one-dimensional approximation of the Navier–Stokes equation, J. Fluid Mech. 246 (1994) 205–221.
[19] S.P. Lin, Z.W. Lian, Absolute instability of a liquid jet in a gas, Phys. Fluids A 1 (1989) 490–499.
[20] M.H.I. Baird, J.F. Davidson, Annular jets – I, fluid dynamcis, Chem. Eng. Sci. 17 (1962) 467–472.
[21] J.B. Keller, M.L. Weitz, Upward 'falling' jets and surface tension, J. Fluid Mech. 2 (1957) 201–203.
[22] J.I. Ramos, Upward and downward annular liquid jets: conservation properties, singularities and numerical errors, Appl. Math. Modell. 20 (1996) 440–458.
[23] D.S. Finnicum, S.J. Weinstein, K.J. Ruschak, The effect of applied pressure on the shape of a two-dimensional liquid curtain falling under the influence of gravity, J. Fluid Mech. 255 (1993) 647–665.
[24] D.R. Lide, Handbook of Chemistry and Physics, CRC Press, United Kingdom, 1997.
[25] D.C.Y. Wong, M.J.H. Simmons, A.C. King, S.P. Decent, E.I. Părău, Dynamic break-up and drop formation from a liquid jet spun from a rotating orifice. Part I: experimental, in: Proceedings of the FEDSM'03: 4th ASME-JSME Joint Fluids Engineering Conference, Honolulu, Hawaii, USA, 2003.
[26] S.P. Decent, A.C. King, The Recoil of a Broken Liquid Bridge, IUTAM Free-Surface Flows, Kluwer, 1997.
[27] C. Clasen, J. Eggers, M.A. Fontelos, J. Li, G.H. McKinley, The beads-on-a-string structure of viscoelastic threads, J. Fluid Mech. 556 (2006) 283–308.
[28] D.H. Peregrine, G. Shoker, A. Symon, The bifurcation of liquid bridges, J. Fluid Mech. 212 (1990) 25–39.